



Electron-beam-induced charging of an Al₂O₃ nanotip studied using off-axis electron holography

Fengshan Zheng^{a,b,*}, Marco Beleggia^c, Vadim Migunov^{a,d}, Giulio Pozzi^{a,e},
Rafal E. Dunin-Borkowski^a

^a Ernst Ruska-Centre for Microscopy and Spectroscopy with Electrons and Peter Grünberg Institute, Forschungszentrum Jülich, 52425 Jülich, Germany

^b Spin-X Institute, School of Physics and Optoelectronics, State Key Laboratory of Luminescent Materials and Devices, Guangdong-Hong Kong-Macao Joint Laboratory of Optoelectronic and Magnetic Functional Materials, South China University of Technology, Guangzhou 511442, China

^c DTU Nanolab, Technical University of Denmark, 2800 Kgs. Lyngby, Denmark

^d Central Facility for Electron Microscopy (GFE), RWTH Aachen University, Ahornstrasse 55, 52074 Aachen, Germany

^e Department FIM, University of Modena and Reggio Emilia, via G. Campi 213/a, 41125 Modena, Italy

ARTICLE INFO

Keywords:

Specimen charging
Al₂O₃
Off-axis electron holography
Transmission electron microscopy
Secondary electron emission

ABSTRACT

Electrostatic charging of specimens during electron, photon or ion irradiation is a complicated and poorly understood phenomenon, which can affect the acquisition and interpretation of experimental data and alter the functional properties of the constituent materials. It is usually linked to secondary electron emission, but also depends on the geometry and electrical properties of the specimen. Here, we use off-axis electron holography in the transmission electron microscope to study electron-beam-induced charging of an insulating Al₂O₃ nanotip on a conducting support. The measurements are performed under parallel electron illumination conditions as a function of specimen temperature, electron dose, primary electron energy and surface cleanliness. We observe a lack of reproducibility of charge density measurements after cycling the specimen temperature. Surprisingly, we find both positively and negatively charged regions in closely adjacent parts of the specimen.

1. Introduction

The phenomenon of electrostatic charging of poorly-conducting or poorly-electrically-contacted specimens in the electron microscope has been discussed in the literature since at least the early 1960s (e.g., [1,2]). It is believed to occur when the inelastic scattering of electrons leads to secondary electron (SE) emission. This process has been investigated much more intensively in the scanning electron microscope (SEM) (e.g., [3]) than in the transmission electron microscope (TEM), where specimens are typically thinner and primary electron energies are higher.

In recent years, charging of biological specimens has attracted increasing interest in cryo-microscopy (e.g., [4,5]), as it can result in a strong degradation of image quality and, therefore, a loss of spatial resolution. Some studies have focused on charging of C films used either as supports for biological specimens (e.g., [4,5]) or as electrostatic phase plates (e.g., [6]). Charging effects in C films are sometimes associated with the “bee-swarm effect” [1], which is also referred to as the “Berriman effect” in biological electron microscopy [4,7–9]. While it is generally expected that SE emission in a TEM leads to a

positively-charged state of the sample, studies have also shown that negatively-charged states may exist in TEM specimens, suggesting that SE emission is not the only mechanism involved in charging [6,10–15].

The effects of specimen charging can include position-dependent image distortion and astigmatism, motion of irradiated areas of the specimen and strong contrast at sharp or broken edges of the sample. Theoretical analyses of microscopic charging mechanisms, in particular by Cazaux [16–20], do not yet provide a complete description of the phenomenon.

A phase contrast transfer function method has been used to measure the phase shift induced by the electrostatic potential due to charging [21,22]. Although several off-axis electron holography studies of charging in the TEM have also been performed [23–26], they have been limited to simple scenarios and have not addressed the role of the environment on the surface of the specimen.

Systematic quantitative measurements of specimen charging are essential to understand the mechanisms of charging in thin specimens that have different electrical properties and geometries, as well as to establish how to reduce charging effects when imaging using both low

* Corresponding author at: Ernst Ruska-Centre for Microscopy and Spectroscopy with Electrons and Peter Grünberg Institute, Forschungszentrum Jülich, 52425 Jülich, Germany.

E-mail address: f.zheng@fz-juelich.de (F. Zheng).

<https://doi.org/10.1016/j.ultramic.2022.113593>

Received 4 January 2022; Received in revised form 16 July 2022; Accepted 21 July 2022

Available online 29 July 2022

0304-3991/© 2022 The Author(s). Published by Elsevier B.V. This is an open access article under the CC BY-NC-ND license (<http://creativecommons.org/licenses/by-nc-nd/4.0/>).

and high energy electrons. Here, we use off-axis electron holography to study charging in an insulating Al_2O_3 nanotip on a conducting support as a function of specimen temperature, electron dose, primary electron energy and surface cleanliness.

2. Experimental methods

Off-axis electron holography [27,28] is an interferometric technique based on the superposition of an object wave that travels through a region of interest of the sample with a reference wave that travels through a nearby region of vacuum. The resulting interference pattern in the image plane carries information about the phase and amplitude of the object electron wave, which can be retrieved by suitable algorithms. The technique has been used to map long-range electrostatic and magnetic fields [29–33]. It should be noted that care is required in such experiments if the reference wave is perturbed by fringing fields that originate from the sample itself [34].

In the absence of magnetic fields and assuming that dynamical diffraction can be neglected, the phase of the object wave can be written in the form

$$\varphi(x, y) = C_E \int_{-\infty}^{+\infty} (V_Q(x, y, z) + V_{MIP}(x, y, z)) dz, \quad (1)$$

where z is the incident electron beam direction, V_Q and V_{MIP} are the contributions to the electrostatic potential from all charges and from the mean inner potential (MIP) of the specimen [35], respectively and C_E is an interaction constant that takes a value of 6.53×10^6 rad/(V m) for 300 kV electrons. By making use of Gauss' law, the (cumulative) projected charge distribution in the specimen can be obtained from a recorded phase image by using the expression [25,36]

$$Q_C = -\frac{\epsilon_0}{C_E} \oint_{\partial C} \nabla \varphi(x(l), y(l)) \cdot \mathbf{n}(x(l), y(l)) dl, \quad (2)$$

where ϵ_0 is the vacuum permittivity, C is a chosen region of integration, ∂C denotes its boundary, ∇ is a two-dimensional gradient operator, Q_C is the total charge present in a Gaussian volume of space that is defined by an infinite (along the z axis) cylinder whose cross-section is C , l is a curvilinear coordinate along ∂C and \mathbf{n} is the outward normal to it. The MIP contribution to a recorded phase image typically has to be removed before performing such a calculation, as it can introduce "artificial" charges at specimen edges, interfaces and thickness gradients, even though its contribution to the total charge in an entire specimen is always zero [26,37]. This approach has been applied successfully to measure charge distributions in a variety of specimens [25,36–38].

3. Experimental details

In the present work, we study a nanotip comprising an insulating apex (Al_2O_3) and a conducting base (Cr_2AlC). Cr_2AlC belongs to the subset of ternary metal carbides that have the general formula $\text{M}_{n+1}\text{AX}_n$ (M: early transition metals, A: A group element, X: C or N) and are referred to as MAX phases. Some ceramics that belong to this family (e.g., Cr_2AlC) possess self-healing properties [39]. The products of oxidation, such as Al_2O_3 and other oxides, have been shown to fill crack sites, thereby effectively healing them. Here, this material, in which Al_2O_3 is an insulator and the MAX phase is a conductor [40], is used to investigate specimen charging in the TEM.

A nanotip was prepared using focused ion beam milling in an FEI Helios NanoLab 460F1 dual beam system. Details of materials synthesis and nanotip preparation can be found elsewhere [41].

Off-axis electron holography experiments were performed at 300 and 60 kV in an FEI Titan 60–300 microscope equipped with a high brightness field emission gun and an electrostatic biprism. The biprism wire was always nearly perpendicular to the axis of the nanotip and was electrically biased at 100 V. In this case, under elliptical illumination, the major axis of the elliptical beam was perpendicular to the axis of the nanotip. This means that the electron beams always touched

the apex and part of the conducting base, excluding the part connecting to the half Cu grid (ground). Off-axis electron holograms were acquired using a direct electron detection Gatan K2-IS 4k×4k camera when the microscope was operated at 300 kV. The interference fringe spacing was 2.4 nm (5.4 pixels), resulting in a spatial resolution of approximately 5 nm in reconstructed phase images, as defined by the size of the mask applied during hologram reconstruction. The width of the interference region was approximately 1.5 μm . An Ultrascan 2k×2k charge-coupled detector (CCD) camera was used in Sections 4.2 and 4.3. The width of the interference region was approximately the same as that above. Reference holograms were recorded from vacuum after moving the specimen away from the field of view (FOV). Digital reconstruction of the holograms was performed using a standard Fourier-transform-based approach implemented in Holoworks software (Gatan, Inc.). Phase images after reconstruction were unwrapped to avoid 2π jumps. The only unwrapping errors occur inside the nanotip, where the unwrapped phase is not trustworthy and is not used in the discussion. If not otherwise specified, phase contour maps, which show equiphase lines, were plotted by calculating $1 + \cosine$ of the phase multiplied by 4. During off-axis electron holography experiments, the specimen temperature was controlled using a double-tilt liquid-nitrogen-cooled specimen holder (Gatan model 636), which can be used to vary the specimen temperature between -180 and $+110$ °C.

High-angle annular dark-field (HAADF) scanning transmission electron microscopy (STEM) imaging and energy dispersive X-ray spectroscopic (EDXS) elemental mapping experiments were performed at 200 kV using an FEI Titan 80–200 ChemiSTEM microscope equipped with a high brightness field emission gun, a probe C_s corrector and a super-X EDXS detector.

4. Results

The nanotip studied here had a length of $\sim 20 \mu\text{m}$, a diameter of ~ 90 nm at its apex (marked by red dashed lines in Fig. 1) and a diameter of $1.5 \mu\text{m}$ at its base. The elemental maps shown in Fig. 1b–e highlight the presence of a chevron-like Cr-rich region, which is marked by cyan dashed lines in each image. A region of $(\text{Al}, \text{Cr})_2\text{O}_3$ is also present at the very apex of the nanotip, as marked by red dashed lines. Additional precipitates (possibly Cr oxides) are also seen in the Al_2O_3 region, as marked by a red arrow in Fig. 1a. The elemental maps were recorded after the charging experiments that are described below had been completed, in order to avoid potential changes to the charge/surface state of the nanotip resulting from illumination by a focused STEM probe.

4.1. Temperature dependence

Fig. 2 shows phase images and corresponding phase contour maps recorded from the nanotip using off-axis electron holography at different temperatures in sequence, measured at 300 kV. The holograms were acquired using a dose rate of $\sim 2.6 e/\text{\AA}^2/\text{s}$ using an exposure time of 8 s. These conditions resulted in a high signal-to-noise ratio in the reconstructed phase images. The measured phase shifts, which decrease from the apex of the nanotip into the surrounding vacuum, suggest the presence of positive charge at the apex of the nanotip at all specimen temperatures. This observation is consistent with a SE charging mechanism. It should be noted that no dependence of specimen charging on electron dose or dose rate was observed over the studied temperature range of between -180 and $+80$ °C.

The results show that initially, at room temperature, almost concentric phase contours are present around the apex of the nanotip (Fig. 2a), suggesting that charge accumulates primarily in this region. This observation does not necessarily indicate that the charge was induced by electron beam illumination, as there is no access to the state when the electron beam was switched off. Corresponding phase maps recorded after heating the nanotip to 50 and 80 °C are shown in Fig. 2b and c,

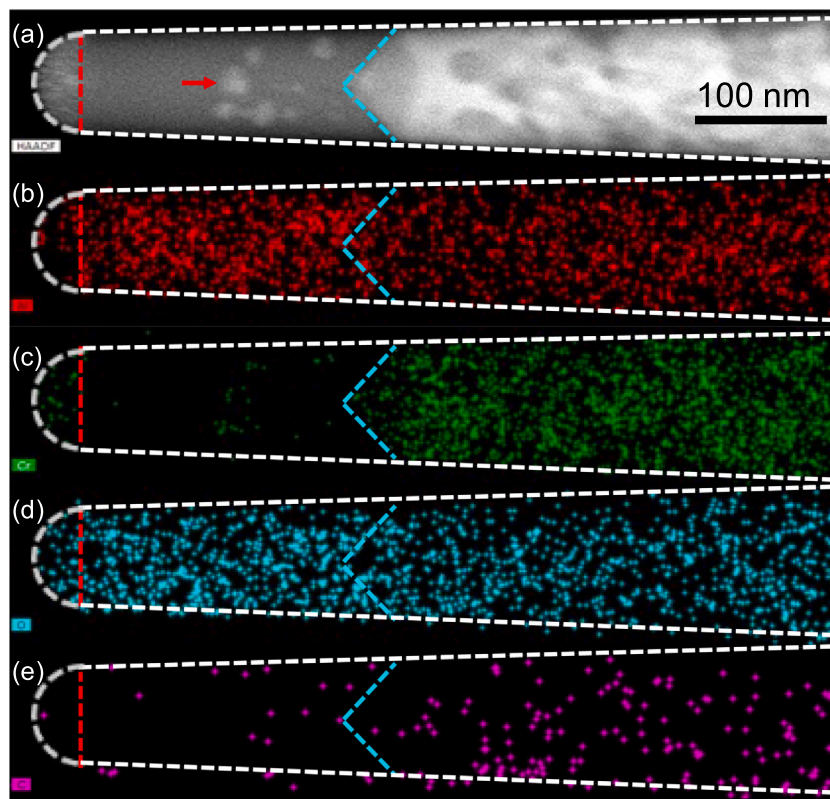


Fig. 1. Chemical characterization of the $\text{Cr}_2\text{AlC-Al}_2\text{O}_3$ nanotip. (a) STEM HAADF image. (b)–(e) EDXS elemental maps of Al, Cr, O and C, respectively. White dashed lines mark the outline of the nanotip. Cyan dashed lines mark the interface between Al_2O_3 and Cr_2AlC . Red dashed lines mark the interface between $(\text{Al}, \text{Cr})_2\text{O}_3$ at the apex and Al_2O_3 . The red arrow in (a) marks the positions of nanoprecipitates, which are thought to be chromium oxides.

respectively. The amount of charge present at the apex of the nanotip can be seen to decrease monotonically with increasing temperature. On the assumption that the SE yield is approximately independent of temperature, this observation suggests that the electrical conductivity of the nanotip increases at higher temperature, allowing the induced charges to be compensated more easily from the conducting base.

Surprisingly, when the nanotip was cooled back to room temperature (Fig. 2d), the charge remained almost the same as at 80 °C (Fig. 2c). Since the effect of temperature on electrical conductivity should be reversible, this observation suggests that the surface or defect state of the sample changed irreversibly during the acquisition of off-axis electron holograms as a function of temperature. It may also suggest the deposition of conductive C contamination at the apex during the cooling process.

When the nanotip was then cooled to -180 °C (Fig. 2e), the number of phase contours increased, indicating stronger charging of the apex of the nanotip, presumably again resulting from the temperature dependence of its electrical conductivity. Subsequently, the nanotip was heated to room temperature (Fig. 2f), resulting in a lower amount of charge than at any previous temperature. Remarkably, when the nanotip was taken back to 80 °C (Fig. 2g), the charge at its apex disappeared almost completely. This charge state then persisted when the nanotip was cooled back down to room temperature (Fig. 2h) using the same approach as in the first cooling iteration from 80 °C to room temperature (Fig. 2c–d).

Since the charge in the specimen was almost absent in the final stages of this cycle, the phase image shown in Fig. 2h was used to subtract the MIP contribution to the phase from the other phase images in the data set. In this way, “artificial” charges associated with variations in the MIP and specimen thickness in the tip could be eliminated [26]. It should be noted that heating/cooling cycles of the specimen may change the MIP. Although such changes may affect the analysis of

charge distributions inside the nanotip, they do not affect the analysis of cumulative charge distributions, since the MIP contribution to the total charge is zero [26]. The resulting phase difference images were used to obtain cumulative charge profiles using Eq. (2).

Cumulative charge profiles were calculated from the phase images recorded at room temperature (Fig. 2a) and -180 °C (Fig. 2e) and are shown in Fig. 3. The integration area used to measure the cumulative charge is marked by a rectangle in the inset in Fig. 3. The size of the integration area was gradually decreased by shrinking it from the left side to the right side, as marked by a white arrow. Both profiles show an increase in the total charge, before a sharp decrease towards the vacuum region. The results suggest that the integration area contains regions that have charge of different polarity, comprising negative charge further from the apex and positive charge closer to the apex. The peak in the profiles is 200–250 nm from the end of the apex, which is consistent with the length of the apex region and suggests that the polarity of the charge changes close to the interface with the conductive base. At room temperature (red profile in Fig. 3) there is a deficit of approximately 115 electrons in the apex of the nanotip, while at -180 °C (blue profile in Fig. 3) there is a deficit of approximately 140 electrons. On the assumption that both profiles start at approximately the same value, it can be concluded that the conductive base is less negatively-charged at room temperature than at -180 °C. It is interesting to note that, to within the measured precision, the profiles show a linear decrease in the apex region, which is consistent with the expected line charge model for an ellipsoidal needle shape [42,43].

4.2. Surface cleanliness

In order to assess the reproducibility of the results presented above, the charge state in the nanotip was checked after several days. Unexpectedly, when using parallel illumination with a dose rate of approximately $2.6 \text{ e}/\text{\AA}^2/\text{s}$ (as in the above results), specimen charging was

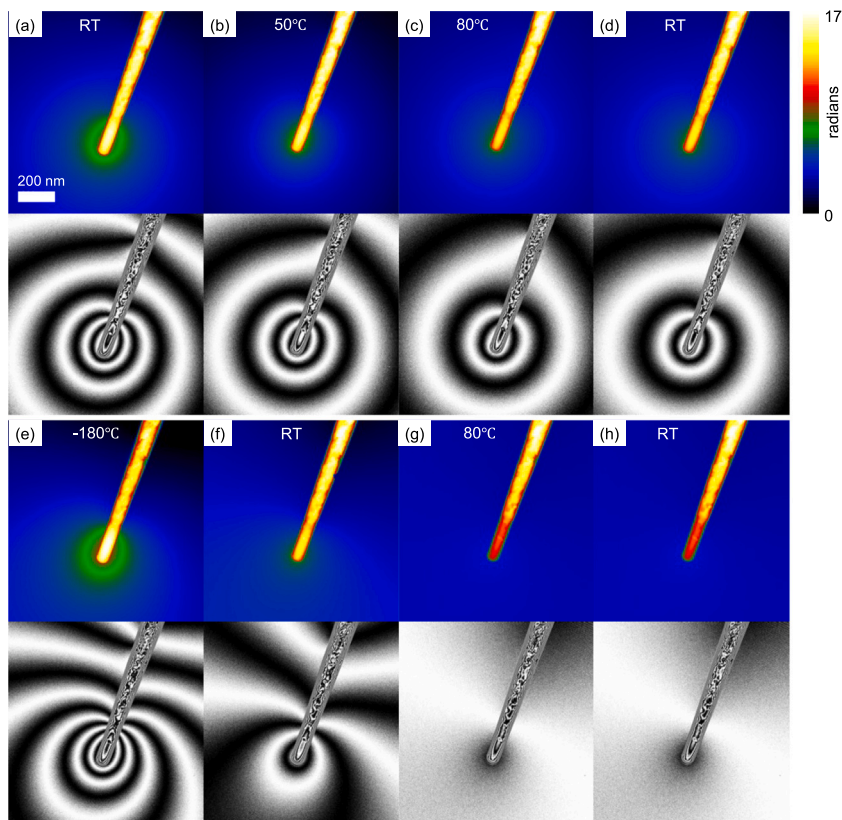


Fig. 2. Off-axis electron holography of electron-beam-induced charging of the nanotip after the specimen temperature was changed in sequence. The images are shown in the order, in which they were recorded, starting and finishing at room temperature (RT). The first and third rows show phase images. The second and fourth rows show corresponding phase contour maps. The contour spacing is $\frac{2\pi}{4}$ rad.

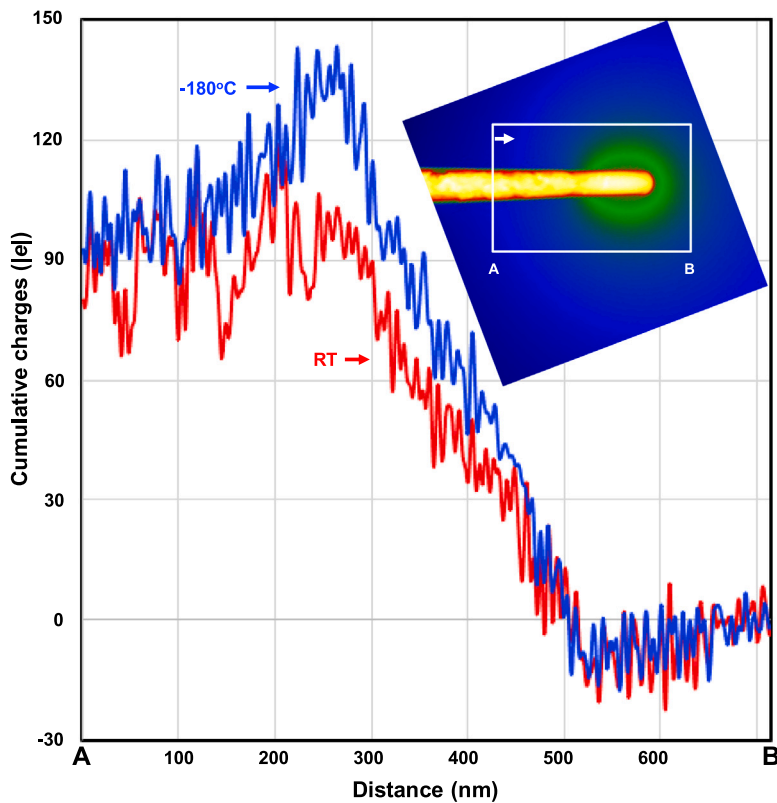


Fig. 3. Cumulative charge profiles determined from the phase images recorded at room temperature (Fig. 2a) and at -180°C (Fig. 2e) using Eq. (2). The integration area, which is marked by a rectangle in the inset, shrinks in the direction marked by a white arrow. The MIP contribution to the phase was subtracted using the phase image shown in Fig. 2h.

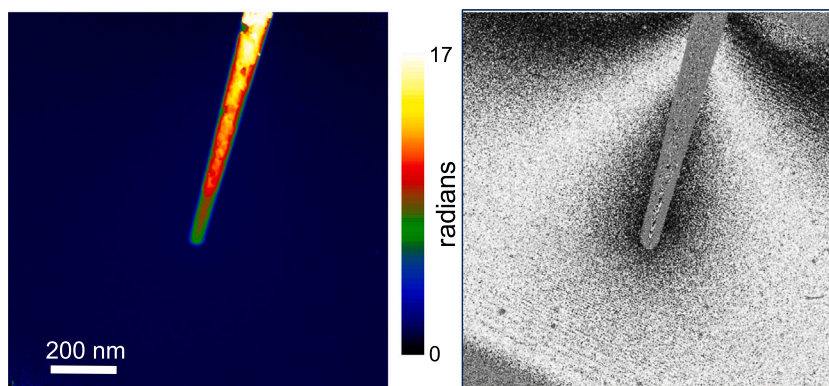


Fig. 4. Off-axis electron holography of electron-beam-induced charging of the nanotip after exposure to air. The nanotip was illuminated by 300 kV electrons at a dose rate of $2.6 \text{ e}/\text{\AA}^2/\text{s}$. A phase image is shown on the left. A corresponding phase contour map is shown on the right. The contour spacing is $\frac{2\pi}{12}$ rad.

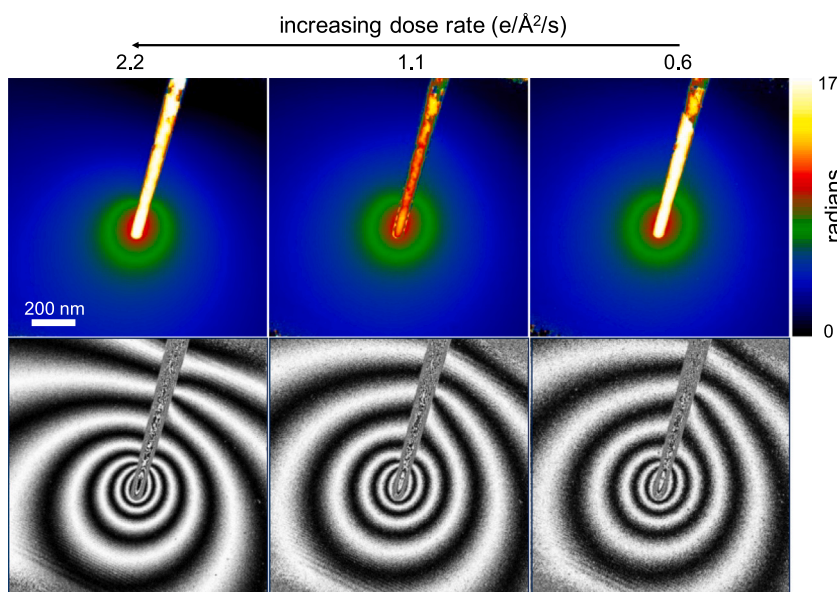


Fig. 5. Off-axis electron holography of electron-beam-induced charging of the nanotip measured at 300 kV after one minute of plasma cleaning. The upper row shows phase images. The lower row shows corresponding phase contour maps. The contour spacing is $\frac{\pi}{4}$ rad. The electron dose rate is indicated above each image.

found to be negligible, as shown in Fig. 4. This observation suggests that either exposure to ambient atmosphere or electron irradiation may have changed the surface or defect state and therefore the charging behaviour of the sample. Little dependence on either dose rate or dose was found, as before.

An attempt was then made to change the surface state of the nanotip by using plasma cleaning (Fischione Instruments, model 1020) with O at a pressure of 10^{-1} mbar, which is expected to remove C, H and O contamination from the specimen surface. Fig. 5 shows measurements of charging of the nanotip after one minute of plasma cleaning. When using similar electron beam illumination conditions and microscope parameters as before, it can be seen that the original charging behaviour of the nanotip had recovered. Little dependence on dose rate (Fig. 5) or total dose was again observed. At a dose rate of $2.2 \text{ e}/\text{\AA}^2/\text{s}$, the phase contours are perpendicular to the axis of the nanotip, whereas at dose rates of 1.1 and $0.6 \text{ e}/\text{\AA}^2/\text{s}$ they are inclined slightly.

It is interesting to note that there is a $\frac{\pi}{2}$ phase shift between the left and right sides of the nanotip (away from the apex), as revealed by bright phase contours on one side connecting to dark contours on the other side. Approximately 2/3 of the distance along the nanotip in the FOV, the $\frac{\pi}{2}$ phase shift disappears. The $\frac{\pi}{2}$ phase shift may be induced by a temporal variation in the charge on the nanotip during electron

exposure. However, corresponding Moiré fringes were not observed in the holograms or reconstructed amplitude images [44].

4.3. Primary electron energy

In order to assess the dependence of specimen charging on primary (incident) electron energy, the accelerating voltage was switched from 300 to 60 kV without taking the sample out of the microscope. Fig. 6 shows the results of charging measurements of the nanotip recorded using 60 kV electrons. Just as at 300 kV, there is little dependence on electron dose rate or total dose.

As a result of the poor quality of the phase inside the nanotip, in particular at 60 kV (when most electrons are not able to penetrate through the specimen), representative phase line profiles were plotted instead of cumulative charge profiles, which may suffer from imperfections of the phase inside the nanotip. Fig. 7 shows representative phase line profiles recorded at different accelerating voltages. The positions of the line profiles are close to and parallel to the axis of the nanotip, as marked by a white line in the inset. The phase shown in Fig. 4 was also plotted for reference. As the interaction constant C_E in Eq. (1) takes a value of $1.14 \times 10^7 \text{ rad}/(\text{V m})$ at 60 kV, while it takes a value of $6.53 \times 10^6 \text{ rad}/(\text{V m})$ at 300 kV, phase images recorded at 60 kV was rescaled by the ratio of C_E at the two accelerating voltages so

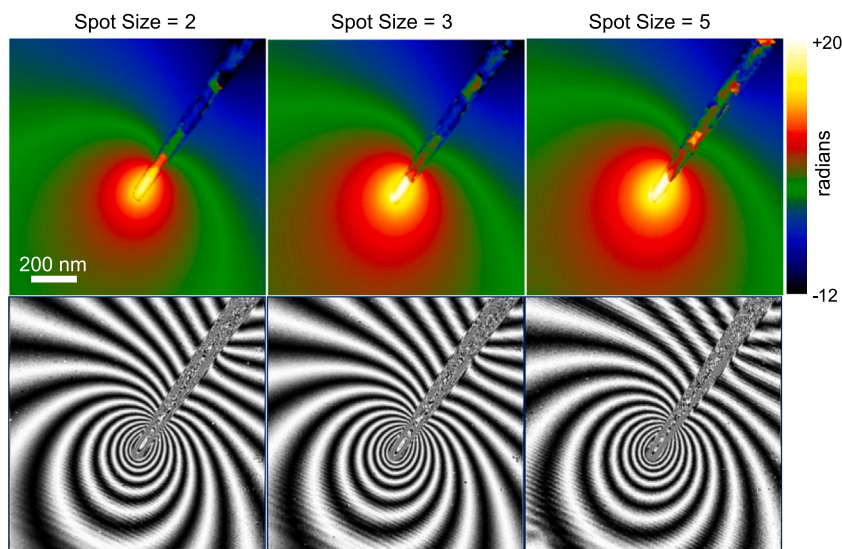


Fig. 6. Off-axis electron holography of electron-beam-induced charging of the nanotip measured at 60 kV. The upper row shows phase images. The lower row shows corresponding phase contour maps. The contour spacing is $\frac{2\pi}{4}$ rad. The electron dose rate is indicated above each image.

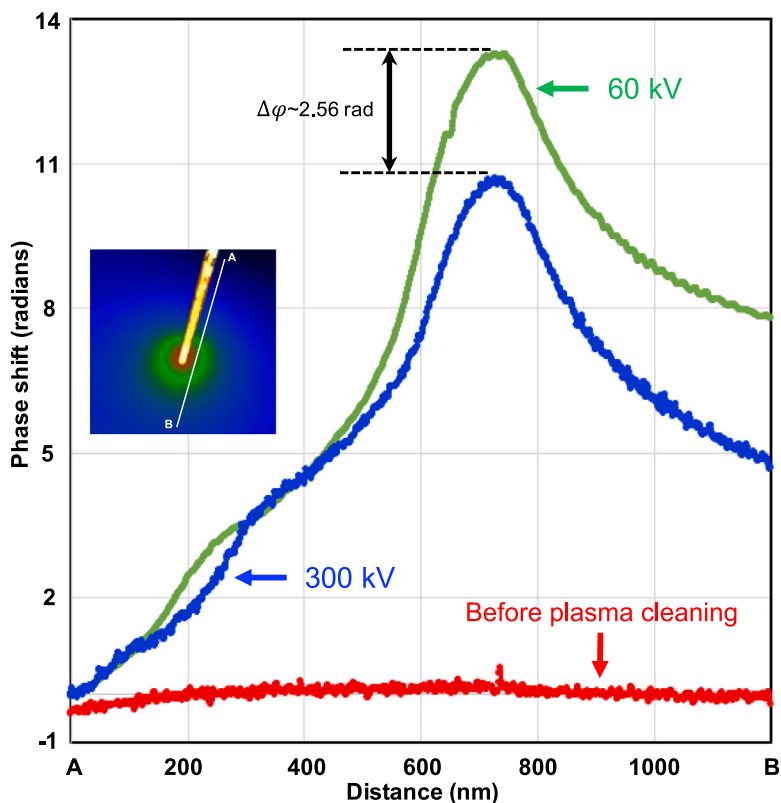


Fig. 7. Representative line profiles taken from phase images recorded after plasma cleaning at 60 kV (green) and 300 kV (blue) and before plasma cleaning at 300 kV (red). The phase shift measured at 60 kV is scaled for comparison with the phase shift measured at 300 kV (see text for details). The chosen line, which is parallel to the axis of the nanotip, is marked by a white line in the inset.

that the results could be compared with each other directly via the corresponding potentials or total charges. The reference phase line profile (red in Fig. 7) is almost flat, suggesting there is negligible charging before plasma cleaning, consistent with discussion in Section 4.2. At 60 kV (green profile), the scaled maximum phase shift is approximately 2.56 rad higher than that at 300 kV (blue profile). Both profiles show a similar behaviour. The results suggest that a lower primary electron energy results in the nanotip becoming more strongly

charged. This behaviour is expected, as the yield of SE emission is inversely proportional to primary electron energy [3,45].

5. Discussion

The polarity of the electron-beam-induced charge (*i.e.*, positive) that we observe experimentally using off-axis electron holography in the insulating apex of the nanotip and its dependence on primary electron energy are consistent with predictions for SE emission, while the lack

of dependence of the amount of charge on electron dose rate and total electron dose is unexpected. The dependence of the amount of charge on specimen temperature may be explained by changes in the conductivity of the conducting base of the nanotip, while the lack of reproducibility following successive cycles of heating and cooling suggests that changes in temperature may alter the surface or defect state of the sample. Changes in electron-beam-induced charging of the nanotip observed after plasma cleaning suggest that the build-up of C on the specimen surface may play a decisive role, highlighting the need to have better control over the cleanliness of sample surfaces in all TEM experiments. The complexity of the present sample, including its geometry, morphology and the presence of damage or ion implantation from sample preparation, makes the measured charge state difficult to model theoretically.

Future experiments will benefit from the examination of ultra-clean samples of simple geometry (e.g., a sphere or a cube), with known conductivity and a known (i.e., Schottky or Ohmic contact) contact to ground, as well as from the use of a well-controlled environment (ultra-high vacuum, O, H₂O or even liquids) and from the systematic variation of specimen temperature, primary electron energy, electron dose and applied electrical bias. The simultaneous measurement of electron optical phase, X-ray emission, SE emission and electron energy-loss spectroscopy, both with high temporal resolution and in coincidence, is also required to fully understand the underlying mechanisms of SE emission and electron-beam-induced charging. An additional complication in such measurements is that they are expected to depend on whether parallel or focused electron beam illumination is used.

6. Summary and conclusions

Electron-beam-induced charging of a nanotip comprising an insulating Al₂O₃ apex on a conducting Cr₂AlC base has been studied using off-axis electron holography as a function of specimen temperature, electron dose rate and total dose, surface cleanliness and primary electron energy. Secondary electron emission, the electrical conductivity and the surface state of the sample are found to play important roles in the charging process. However, the role of intrinsic and electron-beam-induced defects remains unknown. Improved control and knowledge of the specimen geometry, surface state, electrical contact and surrounding environment are required to understand and interpret charging behaviour resulting from electron irradiation. New experimental approaches to mitigate the effects of specimen charging in the transmission electron microscope are also required.

Declaration of competing interest

The authors declare that they have no known competing financial interests or personal relationships that could have appeared to influence the work reported in this paper.

Data availability

Data will be made available on request.

Acknowledgements

The authors are grateful to Prof. Michael Farle and AG Farle at the University of Duisburg–Essen for technical help, Dr. K. G. Pradeep for providing bulk specimens, Maximilian Kruth for focused ion beam specimen preparation, Werner Pieper and Rolf Speen for technical assistance and Gatan, Inc. for cooperation within the framework of a scientific agreement. The authors acknowledge the European Union for funding through the Marie Curie Initial Training Network—SIMDALEE2 (Grant No. 606988 under FP7-PEOPLE-2013-ITN) and through the Horizon 2020 Research and Innovation Programme under Grant agreement No. 823717-ESTEEM3. V. M. thanks the Deutsche

Forschungsgemeinschaft, Germany for funding within the framework of the SFB 917 project NanoSwitches. R. E. D.-B. thanks the Deutsche Forschungsgemeinschaft, Germany for a Deutsch-Israelische Projektkooperation (DIP) Grant and the European Union's Horizon 2020 Research and Innovation Programme Q-SORT (Grant No. 766970 under H2020-FETOPEN-2016-2017).

References

- [1] D. Dove, Image contrasts in thin carbon films observed by shadow electron microscopy, *J. Appl. Phys.* 35 (5) (1964) 1652–1653.
- [2] G. Curtis, R. Ferrier, The electric charging of electron-microscope specimens, *J. Phys. D: Appl. Phys.* 2 (7) (1969) 1035.
- [3] L. Reimer, *Scanning Electron Microscopy: Physics of Image Formation and Microanalysis*, Vol. 45, Springer, 2013.
- [4] C. Russo, R. Henderson, Charge accumulation in electron cryomicroscopy, *Ultramicroscopy* 187 (2018) 43–49.
- [5] C. Russo, R. Henderson, Microscopic charge fluctuations cause minimal contrast loss in cryoEM, *Ultramicroscopy* 187 (2018) 56–63.
- [6] M. Malac, M. Beleggia, M. Kawasaki, P. Li, R. Egerton, Convenient contrast enhancement by a hole-free phase plate, *Ultramicroscopy* 118 (2012) 77–89.
- [7] J. Berriman, K. Leonard, Methods for specimen thickness determination in electron microscopy: II. Changes in thickness with dose, *Ultramicroscopy* 19 (4) (1986) 349–366.
- [8] J. Brink, M. Sherman, J. Berriman, W. Chiu, Evaluation of charging on macromolecules in electron cryomicroscopy, *Ultramicroscopy* 72 (1–2) (1998) 41–52.
- [9] K. Downing, M. McCartney, R. Glaeser, Experimental characterization and mitigation of specimen charging on thin films with one conducting layer, *Microsc. Microanal.* 10 (6) (2004) 783–789.
- [10] R. Danev, B. Buijsse, M. Khoshouei, J.M. Plitzko, W. Baumeister, Volta potential phase plate for in-focus phase contrast transmission electron microscopy, *Proc. Natl. Acad. Sci.* 111 (44) (2014) 15635–15640.
- [11] M. Malac, S. Hettler, M. Hayashida, M. Kawasaki, Y. Konyuba, Y. Okura, H. Iijima, I. Ishikawa, M. Beleggia, Computer simulations analysis for determining the polarity of charge generated by high energy electron irradiation of a thin film, *Micron* 100 (2017) 10–22.
- [12] S. Hettler, E. Kano, M. Dries, D. Gerthsen, L. Pfaffmann, M. Bruns, M. Beleggia, M. Malac, Charging of carbon thin films in scanning and phase-plate transmission electron microscopy, *Ultramicroscopy* 184 (2018) 252–266.
- [13] S. Hettler, J. Onoda, R. Wolkow, J. Pitters, M. Malac, Charging of electron beam irradiated amorphous carbon thin films at liquid nitrogen temperature, *Ultramicroscopy* 196 (2019) 161–166.
- [14] O.A. Dicks, J. Cottom, A.L. Shluger, V.V. Afanas'ev, The origin of negative charging in amorphous Al₂O₃ films: The role of native defects, *Nanotechnology* 30 (20) (2019) 205201.
- [15] K. Harada, M. Malac, M. Hayashida, K. Niitsu, K. Shimada, D. Homeniuk, M. Beleggia, Toward the quantitative the interpretation of hole-free phase plate images in a transmission electron microscope, *Ultramicroscopy* 209 (2020) 112875.
- [16] J. Cazaux, Some considerations on the electric field induced in insulators by electron bombardment, *J. Appl. Phys.* 59 (5) (1986) 1418–1430.
- [17] J. Cazaux, Correlations between ionization radiation damage and charging effects in transmission electron microscopy, *Ultramicroscopy* 60 (3) (1995) 411–425.
- [18] J. Cazaux, Some considerations on the secondary electron emission, δ , from e-irradiated insulators, *J. Appl. Phys.* 85 (2) (1999) 1137–1147.
- [19] J. Cazaux, E-induced secondary electron emission yield of insulators and charging effects, *Nucl. Instrum. Methods Phys. Res. B* 244 (2) (2006) 307–322.
- [20] J. Cazaux, Secondary electron emission and charging mechanisms in Auger electron spectroscopy and related e-beam techniques, *J. Electron Spectrosc. Relat. Phenom.* 176 (1–3) (2010) 58–79.
- [21] K. Danov, R. Danev, K. Nagayama, Electric charging of thin films measured using the contrast transfer function, *Ultramicroscopy* 87 (2001) 45–54.
- [22] K. Danov, R. Danev, K. Nagayama, Reconstruction of the electric charge density in thin films from the contrast transfer function measurements, *Ultramicroscopy* 90 (2002) 85–95.
- [23] B. Frost, An electron holographic study of electric charging and electric charge distributions, *Ultramicroscopy* 75 (2) (1998) 105–113.
- [24] B. Frost, E. Völkl, On the reliability of quantitative phase measurements by low magnification off-axis image plane electron holography, *Ultramicroscopy* 72 (3–4) (1998) 101–107.
- [25] C. Gatel, A. Lubk, G. Pozzi, E. Snoeck, M.J. Hÿtch, Counting elementary charges on nanoparticles by electron holography, *Phys. Rev. Lett.* 111 (2) (2013) 025501.
- [26] M. Beleggia, L. Gontard, R.E. Dunin-Borkowski, Local charge measurement using off-axis electron holography, *J. Phys. D: Appl. Phys.* 49 (29) (2016) 294003.
- [27] A. Tononura, *Electron Holography*, second ed., in: Springer Series in Optical Sciences, Springer, 1999.
- [28] H. Lichte, M. Lehmann, *Electron holography—basics and applications*, *Rep. Progr. Phys.* 71 (1) (2007) 016102.

- [29] H. Lichte, F. Börrnert, A. Lenk, A. Lubk, F. Röder, J. Sickmann, S. Sturm, K. Vogel, D. Wolf, Electron holography for fields in solids: Problems and progress, *Ultramicroscopy* 134 (2013) 126–134.
- [30] G. Pozzi, M. Beleggia, T. Kasama, R.E. Dunin-Borkowski, Interferometric methods for mapping static electric and magnetic fields, *C. R. Phys.* 15 (2–3) (2014) 126–139.
- [31] D. Shindo, T. Tanigaki, H.S. Park, Advanced electron holography applied to electromagnetic field study in materials science, *Adv. Mater.* 29 (25) (2017) 1602216.
- [32] M.R. McCartney, R.E. Dunin-Borkowski, D.J. Smith, Quantitative measurement of nanoscale electrostatic potentials and charges using off-axis electron holography: Developments and opportunities, *Ultramicroscopy* 203 (2019) 105–118.
- [33] R.E. Dunin-Borkowski, A. Kovács, T. Kasama, M.R. McCartney, D.J. Smith, Electron holography, in: *Springer Handbook of Microscopy*, Springer, 2019, pp. 767–818.
- [34] G. Matteucci, G. Missiroli, M. Muccini, G. Pozzi, Electron holography in the study of the electrostatic fields: the case of charged microtips, *Ultramicroscopy* 45 (1) (1992) 77–83.
- [35] M. O’Keeffe, J. Spence, On the average Coulomb potential (Φ_0) and constraints on the electron density in crystals, *Acta Crystallogr. A* 50 (1) (1994) 33–45.
- [36] M. Beleggia, T. Kasama, R.E. Dunin-Borkowski, S. Hofmann, G. Pozzi, Direct measurement of the charge distribution along a biased carbon nanotube bundle using electron holography, *Appl. Phys. Lett.* 98 (24) (2011) 243101.
- [37] F. Zheng, J. Caron, V. Migunov, M. Beleggia, G. Pozzi, R.E. Dunin-Borkowski, Measurement of charge density in nanoscale materials using off-axis electron holography, *J. Electron Spectrosc. Relat. Phenom.* 241 (2020) 146881.
- [38] V. Migunov, A. London, M. Farle, R.E. Dunin-Borkowski, Model-independent measurement of the charge density distribution along an Fe atom probe needle using off-axis electron holography without mean inner potential effects, *J. Appl. Phys.* 117 (13) (2015) 134301.
- [39] P. Eklund, M. Beckers, U. Jansson, H. Högberg, L. Hultman, The $M_{n+1}AX_n$ phases: Materials science and thin-film processing, *Thin Solid Films* 518 (8) (2010) 1851–1878.
- [40] W. Tian, P. Wang, G. Zhang, Y. Kan, Y. Li, D. Yan, Synthesis and thermal and electrical properties of bulk Cr_2AlC , *Scr. Mater.* 54 (5) (2006) 841–846.
- [41] K. Pradeep, K. Chang, A. Kovács, S. Sen, A. Marshal, R. de Kloe, R. Dunin-Borkowski, J. Schneider, Nano-scale Si segregation and precipitation in $Cr_2Al(Si)C$ MAX phase coatings impeding grain growth during oxidation, *Mater. Res. Lett.* 7 (5) (2019) 180–187.
- [42] G. Matteucci, G.F. Missiroli, G. Pozzi, Electron holography of long-range electrostatic fields, in: P.W. Hawkes (Ed.), *Advances in Imaging and Electron Physics*, Vol. 122, Elsevier, 2002, pp. 173–249.
- [43] M. Beleggia, T. Kasama, D. Larson, T.F. Kelly, R.E. Dunin-Borkowski, G. Pozzi, Towards quantitative off-axis electron holographic mapping of the electric field around the tip of a sharp biased metallic needle, *J. Appl. Phys.* 116 (2) (2014) 024305.
- [44] M. Beleggia, G. Pozzi, Comment on ‘electron holography on dynamic motion of secondary electrons around sciatic nerve tissues’, *J. Electron Microsc.* 57 (5) (2008) 165–167.
- [45] M. Chung, T. Everhart, Simple calculation of energy distribution of low-energy secondary electrons emitted from metals under electron bombardment, *J. Appl. Phys.* 45 (2) (1974) 707–709.